

# Scalar and Tensor Holographic Artificial Impedance Surfaces

Bryan H. Fong, Joseph S. Colburn, *Member, IEEE*, John J. Ottusch, John L. Visher, and Daniel F. Sievenpiper, *Fellow, IEEE*

**Abstract**—We have developed a method for controlling electromagnetic surface wave propagation and radiation from complex metallic shapes. The object is covered with an artificial impedance surface that is implemented as an array of sub-wavelength metallic patches on a grounded dielectric substrate. We pattern the effective impedance over the surface by varying the size of the metallic patches. Using a holographic technique, we design the surface to scatter a known input wave into a desired output wave. Furthermore, by varying the shape of the patches we can create anisotropic surfaces with tensor impedance properties that provide control over polarization. As an example, we demonstrate a tensor impedance surface that produces circularly polarized radiation from a linearly polarized source.

**Index Terms**—Antennas, artificial materials, electromagnetic scattering, holographic gratings, impedance sheets, surface impedance, surface waves.

## I. INTRODUCTION

A common challenge for antenna designers is the integration of antennas onto complex metallic shapes while maintaining the desired radiation characteristics. The antenna excites currents in nearby conductors, and these currents can contribute to unexpected artifacts in the radiation pattern, including shadowing, nulls, cross-polarization, or radiation in undesired directions.

We have developed a method to control the radiation from surface currents on metallic bodies. Our method is based on an artificial impedance surface consisting of a grounded dielectric layer covered with a pattern of conductive patches. The patches are small compared to the electromagnetic wavelength, and we can describe their scattering properties in terms of their effective surface impedance. By varying the size and shape of the patches, we can control the surface impedance as a function of position and direction.

The surface impedance is patterned over the body of interest using a holographic technique [1] in which we calculate the interference pattern between the currents generated by a source and the fields associated with the desired radiation, and design

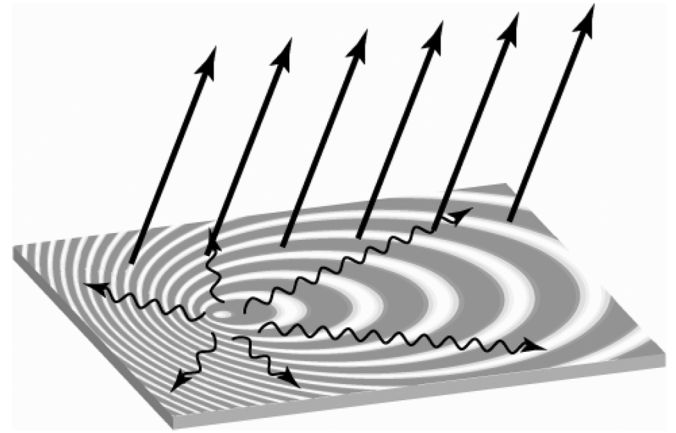


Fig. 1. Holographic leaky wave antenna concept. Surface waves (undulating arrows) are excited on an artificial impedance surface, and are scattered by variations in the surface impedance to produce the desired radiation (straight arrows).

the spatial profile of the surface impedance to match this interference pattern. Currents from the source are scattered by the modulated surface impedance to produce the desired radiation pattern. The source can be a small feed or a plane wave impinging on the body.

The concept of the holographic artificial impedance surface was first introduced in several recent conference papers [2]–[4]. In this work, we expand on the previous publications to provide a detailed explanation of how to design and characterize holographic artificial impedance surfaces, including the equations necessary for others to reproduce our results. We also provide the first measured data for a tensor impedance surface, and demonstrate that such a surface can generate a high gain beam with circularly polarized radiation from a small linearly polarized feed.

Holographic artificial impedance surfaces are based on three established concepts: leaky waves on modulated impedance surfaces, artificial impedance surfaces, and holographic antennas, illustrated in Fig. 1. The foundation for this work is Oliner's comprehensive analysis of leaky waves on modulated impedance surfaces [5] in which he describes how the propagation and radiation of leaky waves are controlled by the magnitude, modulation depth, and period of the surface impedance. We have implemented Oliner's impedance boundary using an artificial impedance surface, and extended the modulation concept using a two-dimensional holographic patterning method. We have also expanded this idea to include anisotropic or tensor impedance surfaces which can control polarization.

Manuscript received November 13, 2009; revised February 12, 2010; accepted April 08, 2010. Date of publication July 01, 2010; date of current version October 06, 2010. This work was supported in part by the United States Air Force Office of Scientific Research under Contract FA9550-06-C-0021, The Boeing Company, General Motors, and in part by Raytheon.

B. H. Fong, J. S. Colburn, J. J. Ottusch and J. L. Visher are with HRL Laboratories, LLC, Malibu, CA 90265 USA.

D. F. Sievenpiper was with HRL Laboratories, LLC, Malibu, CA 90265 USA. He is now with the University of California, San Diego, La Jolla, CA 92093-0407 USA (e-mail: sievenpiper@ece.ucsd.edu).

Digital Object Identifier 10.1109/TAP.2010.2055812

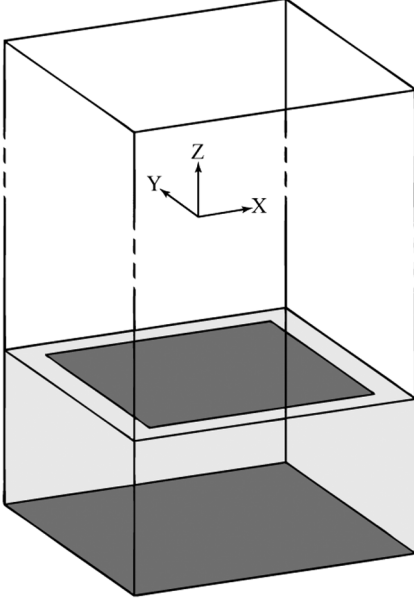


Fig. 2. Unit cell used for scalar impedance surface. A square metal patch sits atop a dielectric layer with a PEC backing. The gap between square patches determines the effective scalar impedance.

## II. ARTIFICIAL IMPEDANCE SURFACES

Various kinds of artificial impedance surfaces have been studied in the past, such as pin-bed structures [6], and high-impedance surfaces [7]. Recently, other kinds of two-dimensional metamaterials have been designed to provide other exotic properties such as left-handed materials [8]–[10]. Because the metallic patterns in these structures are small compared to the wavelength of interest, they can be described as effective media. This permits the analysis of their scattering properties using only the macroscopic effective surface impedance instead of the detailed local geometry, enabling us to model electrically large structures based on these artificial materials using practical computing hardware.

Our artificial impedance surface is based on a square lattice of sub-wavelength conductive patches on a grounded dielectric substrate. Because the structure is quasi-periodic, we simulate its effective surface impedance using a single unit cell with periodic boundary conditions, as shown in Fig. 2. This approach assumes that the structure is uniform, but the results can be used to design a non-uniform surface if its properties are slowly varying. For this analysis, we have used both the commercial Ansoft HFSS code, and our proprietary FastScat code [11] that has been adapted to include periodic boundary conditions. The HFSS code is an FEM-based solver, while the FastScat code is a high-order Nyström discretization frequency domain integral equation solver. The surface impedance can be calculated using one of three methods, which are described below.

Using HFSS, we apply periodic boundary conditions to the four vertical walls of the simulation volume. The bottom wall is an electric conductor, and the top wall is a radiation boundary. The simulation also includes a block of dielectric, and a single square conductive patch. The top wall must be sufficiently far from the structure not to affect calculation of bound surface

wave modes, but not so far as to introduce other propagating modes in the free space volume. A practical height for the top wall is about  $1/2$  wavelength. We then solve for the eigenmode that satisfies these boundary conditions to obtain the properties of the surface wave, and extract the effective surface impedance.

The effective surface impedance can be most easily understood as the ratio of the electric to magnetic fields near the surface, averaged over the unit cell. For transverse magnetic waves (TM) propagating in the  $X$  direction, the effective surface impedance is

$$Z = \int_{\text{cell}} \frac{E_x}{H_y} ds. \quad (1)$$

Throughout the paper TM modes have magnetic field transverse to the direction of surface wave propagation; transverse electric (TE) modes similarly have electric field transverse to the direction of propagation.

Since both fields decay away from the surface at the same rate, this ratio is independent of the position above the surface. However the integration should be done at a height that it is sufficiently far from the surface that near-field effects are negligible, yet also sufficiently far from the absorbing boundary condition that it does not affect the calculation of the surface impedance. The midpoint of the simulation volume is a good practical choice.

The surface impedance can also be calculated using another method that does not require integration of the fields. For a bound surface wave, the refractive index  $n$  seen by the wave is the ratio of the speed of light  $c$  in free space to the phase velocity of the wave along the surface,  $n = c/v_{ph} = k_t c/\omega$ , where  $k_t$  is the surface wave wave vector. Using HFSS, we can calculate an eigenfrequency  $\omega$  for a given phase difference  $\phi$  across a unit cell of length  $a$ . Since the phase difference  $\phi$  across the unit cell is related to the wave vector through  $\phi = k_t a$ , the index  $n$  is completely determined. Alternatively, using our FastScat code we can solve for the surface wave wave vector  $k_t$  at frequency  $\omega$ , again determining the index  $n$ . With bound surface waves having the functional dependence  $e^{j\omega t} e^{-j\mathbf{k}_t \cdot \mathbf{x}_t} e^{-k_z z}$ , where the  $t$  subscript denotes quantities in the  $X$ - $Y$  plane, Maxwell's equations and the impedance boundary condition require that the surface impedance for TM modes is related to the decay constant  $k_z$  of the fields away from the surface by [12]

$$Z = jZ_0 \frac{k_z}{k} \quad (2)$$

where  $k = \omega/c$  and  $Z_0$  is the impedance of free space. Notice that the ratio  $k_z/k$  gives the modulus of the surface impedance normalized to the free space impedance; this observation will be important in the analysis of tensor impedance surfaces. The wave equation relates the wave vector  $k_t$  along the surface to the decay constant  $k_z$

$$k_z^2 = k_t^2 - k^2. \quad (3)$$

giving the relationship between the effective refractive index and the effective surface impedance

$$Z = Z_0 \sqrt{1 - n^2}. \quad (4)$$

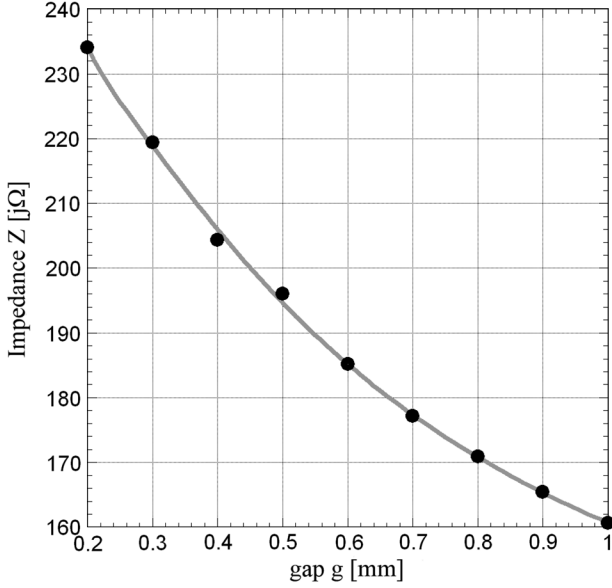


Fig. 3. Plot of impedance  $Z$  versus gap  $g$  at 17 GHz for the unit cell shown in Fig. 1. Points show the result of HFSS calculations, and the line is given by (5). The unit cell has a lattice constant of 3 mm, and the dielectric is 1.57 mm thick with dielectric constant 2.2. For this range of impedance between  $161j\Omega$  and  $234j\Omega$ ,  $X$  and  $M$  in (8) take the values  $197.5\Omega$  and  $36.5\Omega$ , respectively.

This expression is used for transverse magnetic waves, and a similar expression can be derived for TE waves. This method produces the same result as integrating the fields, but is much simpler because it only requires calculating the surface wave frequency or wave vector.

A third method involves calculating the reflection coefficient of the surface, and extracting the sheet impedance of the metallic layer. The sheet impedance, and the properties of the dielectric layer are then used to calculate the effective surface impedance [13].

As a general rule, higher impedance values are obtained with a narrower gap, a higher dielectric constant substrate, a thicker substrate, or a larger period. However, one must take care to ensure that the period does not exceed the effective medium limit, and that the substrate is sufficiently thin to suppress higher order modes.

As an example, we have analyzed a structure based on 1.57 mm thick Rogers Duroid 5880, with a dielectric constant of 2.2, and a lattice constant of 3 mm. For this analysis, we arbitrarily choose a phase difference of 72 degrees per cell for the periodic boundary conditions. The choice of phase difference determines the location on the dispersion curve, and affects the frequency of operation. By sweeping the size of the gaps between the metal patches, we determined the impedance as a function of the gap width using HFSS. For gaps ranging from 1 mm to 0.2 mm, the effective impedance varied from  $161j$  to  $234j$  ohms at 17 GHz, plotted in Fig. 3. Using the HFSS computed impedance data, we computed a least-squares fit to the impedance as a function of the inverse gap:

$$Z = j \left( 107 + \frac{65.5}{g} - \frac{12.7}{g^2} + \frac{0.94}{g^3} \right) \quad (5)$$

Here the impedance is in ohms and the gap  $g$  is in mm.

This function is inverted to give the gap size as a function of desired impedance value. After characterizing the surface impedance for a range of gap sizes, we then build an artificial impedance surface in which the gap and the effective impedance vary as a function of position using our holographic patterning technique.

### III. HOLOGRAPHIC PATTERNING

Originally demonstrated at optical frequencies, holography involves producing an interference pattern using two waves, and then using the interference pattern to scatter one wave to produce the other. In optical holography, one wave is produced by scattering a laser beam from the object to be imaged, and the other is a reference plane wave from the same laser. The interference pattern formed by these two waves is recorded on photographic film. When the reference wave illuminates the developed film, it is scattered by the recorded interference pattern to produce a copy of the original object wave. For a reference wave  $\Psi_{ref}$  and an object wave  $\Psi_{obj}$ , the interference pattern contains a term proportional to  $\Psi_{obj}\Psi_{ref}^*$ . When the interference pattern is illuminated by the reference wave, this term gives

$$(\Psi_{obj}\Psi_{ref}^*)\Psi_{ref} = \Psi_{obj}|\Psi_{ref}|^2 \quad (6)$$

i.e., a copy of the original object wave [1].

Microwave holograms [14], [15] are created using a similar concept. A source antenna produces the reference wave, which can be a surface wave, [16] and the desired radiation pattern corresponds to the object wave. The microwave hologram is built as a collection of scatterers that correspond to the interference pattern produced by these two waves, and it scatters the reference wave to produce the object wave. In our approach, we implement the hologram as a two-dimensional modulated artificial impedance surface.

The surface impedance is designed by generating the interference pattern between a wave  $\Psi_{surf}$  corresponding to the currents generated by the antenna and a wave  $\Psi_{rad}$  corresponding to the radiation pattern we would like to generate. For a given radiation pattern, the method requires  $\Psi_{rad}$  on the impedance surface, i.e., the near field values of the radiating wave evaluated on the impedance surface. The fidelity of the holographically reproduced far field is of course limited by the size of the impedance surface. As a simple example, assume that we would like to use a small monopole antenna located at the origin on a surface occupying the X-Y plane. The currents generated by this antenna can be approximated as a cylindrical wave

$$\Psi_{surf} = e^{-jk_{nr}} \quad (7)$$

where  $n$  corresponds to the effective index seen by the surface currents, and  $r$  is the radial distance from the antenna. Assume that we would like this antenna to produce a narrow pencil beam in a particular direction  $\theta_L$  in the X-Z plane. The fields on the surface associated with this plane wave radiation pattern are represented by

$$\Psi_{rad} = e^{jk_x \sin(\theta_L) + j\phi} \quad (8)$$

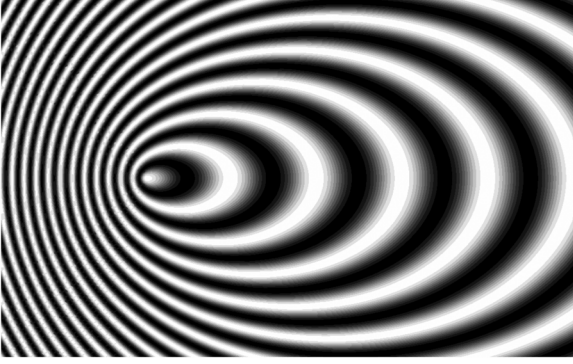


Fig. 4. Scalar impedance pattern formed from holographic interference (8). Impedance values are shown on a linear scale, with light areas corresponding to high impedance. The impedance pattern scatters the surface wave from a point source into a plane wave  $60^\circ$  from the normal.

where  $\phi$  is an arbitrary phase offset that sets the impedance value at the origin. We define the surface impedance as the interference pattern between these two waves

$$Z(\mathbf{x}_t) = j [X + M \operatorname{Re}(\Psi_{rad} \Psi_{surf}^*)] \quad (9)$$

where  $X$  is an arbitrary real average value,  $M$  is the real modulation depth, and  $\mathbf{x}_t$  is a point on the impedance surface in the X-Y plane. As in the optical holography case, the radiated (object) wave results from the scattering of the surface wave from the modulated impedance, given by  $\Psi_{rad} |\Psi_{surf}|^2$ . The hologram pattern shown in Fig. 4 is the interference pattern formed by a point source and a plane wave propagating 60 degrees from normal. In practice, we typically set  $X$  to the average impedance value for the geometry of choice, and we set  $M$  to span the entire available impedance range. However, since the radiation rate is proportional to  $M$ , it can be adjusted depending on the size of the surface to obtain a desired aperture profile.

The holographic pattern shown in Fig. 4 is combined with the impedance data shown in Fig. 3 to determine the required gap as a function of position. We combined (5) with (9) to produce a function describing the gap size versus position on the surface, and used this to produce a file describing a pattern of squares. These squares were then printed as metal patches on a 25.4 cm (Y-dimension) by 40.64 cm (X-dimension) 1.6 mm thick (Z-dimension) Duroid 5880 printed circuit board. A small section of the pattern of metal squares is shown in Fig. 5.

The surface was fed by a 3 mm long monopole antenna inserted from the back, located at the focus of the ellipses shown in Fig. 4. Currents generated by the monopole are scattered by the holographic impedance surface to produce a narrow pencil beam at  $\theta_L = 60$  degrees with a measured gain of about 20 dBi, as shown in Fig. 6, which plots the measured  $\theta$  polarized radiation pattern in the X-Z plane. For comparison, a monopole on a similar smooth metal surface produces the expected low-gain pattern, shown on the same plot. Thus, the holographic impedance surface has scattered the surface wave to produce the desired plane wave, with little of the feed energy being directly radiated into free space.

This example involves TM waves propagating on an inductive impedance surface to produce vertically polarized radiation. A similar result can be obtained with TE waves on a capacitive

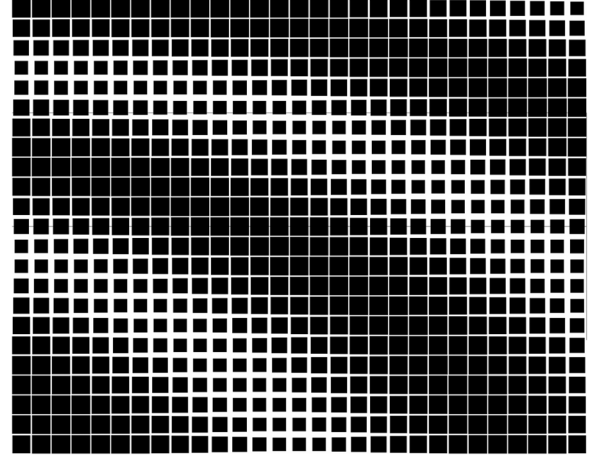


Fig. 5. A portion of the holographic pattern of Fig. 3 implemented using square patches. High impedance regions have small gaps (and are darker). Gaps vary between 0.2 mm and 1 mm, i.e., the full range of gaps and impedances shown in Fig. 2. The unit cell size is fixed at 3 mm. At 17 GHz the free space wavelength is 17 mm.

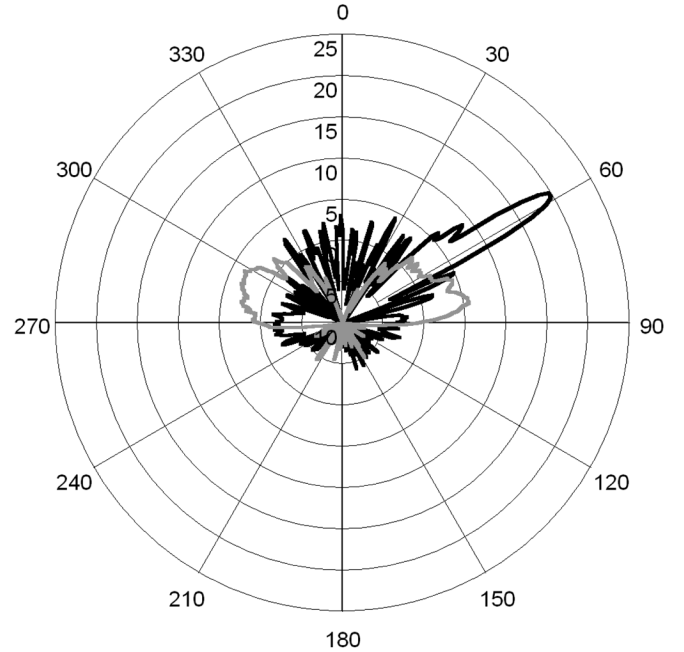


Fig. 6. Measured radiation patterns from monopole antenna placed above the holographic impedance surface (black) and a smooth metal surface (grey). The inclination angle is defined from the impedance surface normal, i.e., the Z-axis, in the X-Z plane.

impedance surface to produce horizontally polarized radiation. To generate arbitrary polarization from any source requires a method of controlling the coupling between currents in any direction and fields in any direction. This requires an anisotropic surface, which can be described using an impedance tensor.

#### IV. ARTIFICIAL TENSOR IMPEDANCE SURFACES

In the scalar impedance case the relationship between impedance and geometrical parameter (metal patch size) is mapped out by determining the bound mode wave number for each value of gap  $g$ . In the tensor impedance case, the relationship between tensor impedance components and geometrical

parameters is similarly determined. We derive an equation relating tensor impedance components to surface wave properties, and we use simulations or measurements to determine the relationship between geometrical patterning and surface wave parameters.

For a uniform surface in the X-Y plane, bound surface waves decay into the surrounding space, and have spatial dependence  $\exp(-j\mathbf{k}_t \bullet \mathbf{x}_t) \exp(-k_z z)$ ; again,  $t$  subscripts refer to in-plane quantities. For scalar impedance surfaces, we divide surface waves into TM, and TE modes, where transversality is with respect to the surface wave propagation direction  $\mathbf{k}_t$ . For TM waves, using the spatial dependence above, the fields are given [12] by (a time dependence of  $e^{j\omega t}$  is assumed throughout)

$$H_{\text{TM}} = \hat{z} \times \mathbf{k}_t e^{-j\mathbf{k}_t \bullet \mathbf{x}_t} e^{-k_z z}, \quad (10.a)$$

$$E_{\text{TM}} = \frac{Z_0}{k} [-\hat{z} k_t^2 - j k_z \mathbf{k}_t] e^{-j\mathbf{k}_t \bullet \mathbf{x}_t} e^{-k_z z}. \quad (10.b)$$

For TE waves, the fields are given by

$$E_{\text{TE}} = Z_0 \hat{z} \times \mathbf{k}_t e^{-j\mathbf{k}_t \bullet \mathbf{x}_t} e^{-k_z z} \quad (11.a)$$

$$H_{\text{TE}} = \frac{1}{k} [\hat{z} k_t^2 + j k_z \mathbf{k}_t] e^{-j\mathbf{k}_t \bullet \mathbf{x}_t} e^{-k_z z}. \quad (11.b)$$

The term  $\mathbf{k}_t = k_x \hat{x} + k_y \hat{y}$  is the transverse wave vector for a wave traveling across the surface at angle

$$\theta_k = \arctan(k_y/k_x). \quad (12)$$

From the wave equation, the terms in the wave vector are related through  $k_x^2 + k_y^2 - k_z^2 = k^2$ . Note that the exponentially decaying dependence in the  $z$  direction results in a negative sign before  $k_z$ .

On a tensor impedance surface, the surface wave modes are in general neither pure TM nor TE, but rather a hybrid. The electric and magnetic fields can thus be written as

$$E = E_{\text{TM}} + \alpha E_{\text{TE}} \quad (13)$$

and

$$H = H_{\text{TM}} + \alpha H_{\text{TE}}. \quad (14)$$

The tensor impedance boundary condition on the  $z = 0$  surface is written as

$$E = \mathbf{Z} \cdot \hat{z} \times H = \mathbf{Z} \cdot J \quad (15)$$

for the tangential components of  $E$  and  $H$ , and the current  $J$ . Energy conservation requires that  $\mathbf{Z}$  be anti-Hermitian, and reciprocity requires that  $\mathbf{Z}$  be pure imaginary [17]. (Notice that this requires  $Z_{xy} = Z_{yx}$ .) Substituting the combined TM and TE fields (13) and (14) into the boundary condition (15) gives

$$\begin{aligned} Z_0 \begin{pmatrix} -j \frac{k_z}{k} \cos \theta_k - \alpha \sin \theta_k \\ -j \frac{k_z}{k} \sin \theta_k + \alpha \cos \theta_k \end{pmatrix} \\ = \begin{pmatrix} Z_{xx} & Z_{xy} \\ Z_{xy} & Z_{yy} \end{pmatrix} \begin{pmatrix} -\cos \theta_k - j \alpha \frac{k_z}{k} \sin \theta_k \\ -\sin \theta_k + j \alpha \frac{k_z}{k} \cos \theta_k \end{pmatrix}. \end{aligned} \quad (16)$$

For a given impedance tensor and propagation direction  $\theta_k$ , we can solve for  $\alpha$  and the  $k_z/k$  ratio. The  $k_z/k$  ratio is

$$\begin{aligned} \frac{k_z}{k} = & \left[ (-j (Z_0^2 - Z_{xy}^2 + Z_{xx} Z_{yy}) \right. \\ & \pm \left\{ - (Z_0^2 - Z_{xy}^2 + Z_{xx} Z_{yy})^2 + 4 Z_0^2 \right. \\ & \times (Z_{yy} \cos^2 \theta_k - Z_{xy} \sin 2\theta_k + Z_{xx} \sin^2 \theta_k) \\ & \times (Z_{xx} \cos^2 \theta_k + Z_{xy} \sin 2\theta_k + Z_{yy} \sin^2 \theta_k) \}^{1/2} \left. \right] \\ & \times [2 Z_0 (Z_{yy} \cos^2 \theta_k - Z_{xy} \sin 2\theta_k + Z_{xx} \sin^2 \theta_k)]^{-1} \end{aligned} \quad (17)$$

where the minus sign corresponds to a TM-like mode, and the plus sign to a TE-like mode. For TM-like modes, the impedance tensor has purely inductive eigenvalues and requires that the negative sign be taken in (17) to produce bound surface waves. Similarly, for TE-like modes, the impedance tensor's purely capacitive eigenvalues requires the plus sign be taken in (17) for bound surface waves. In the scalar impedance case the  $k_z/k$  ratio (2) gives the  $Z_0$ -normalized scalar impedance, which is independent of surface wave propagation direction. In the tensor impedance case we can interpret the  $k_z/k$  ratio as giving an *effective* normalized scalar impedance that is propagation direction dependent. However, this interpretation does not extend to the surface electric field and current since they are not generally aligned. Equation (17) also implies that the mode phase velocity is direction dependent, as is generally true in an anisotropic medium.

Equation (17) expresses the effective normalized scalar impedance as a function of tensor impedance components and propagation direction. To determine the impedance tensor components using (17) requires computing or measuring the effective normalized scalar impedance at three different propagation directions and then solving for the three unknowns  $Z_{xx}$ ,  $Z_{xy}$ , and  $Z_{yy}$  from the three nonlinear constraint equations. If data from more than three different propagation directions is available, a least squares solution to the constraint equations derived from (17) can be used.

The periodic array of metal squares described in the scalar case can be extended to produce a tensor impedance surface by adding a slice through each square, and varying the width  $g_s$  and angle  $\theta_s$  of the slice, as illustrated in Fig. 7. For a surface with given lattice constant, dielectric thickness, and dielectric constant the three independent terms in the impedance tensor,  $Z_{xx}$ ,  $Z_{xy}$ , and  $Z_{yy}$ , are controlled by the three degrees of freedom,  $\theta_s$ ,  $g_s$ , and  $g$ , the width of the gap between the squares.

To understand how the sliced square produces a tensor impedance surface, consider an electric field in the X-direction applied to the square with a diagonal slice. Some portion of the currents in the square will tend to run along the direction of the slice. Thus, the slice provides coupling between currents in the X- and Y-directions and fields in the X- and Y-directions.

Fig. 8 plots the effective normalized scalar impedance as a function of surface wave propagation direction  $\theta_k$ , for the patch geometry shown in Fig. 7, at a frequency of 10 GHz. The effective normalized scalar impedance is computed at  $\theta_k = 60^\circ, 90^\circ, 105^\circ, 120^\circ$  and  $150^\circ$  using FastScat, and the associated

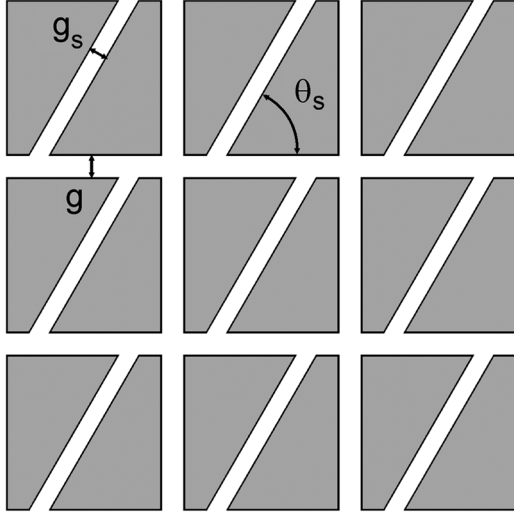


Fig. 7. Unit cells used for tensor impedance surface. A square metal patch with slice sits atop a dielectric layer with a PEC backing. The gap  $g$  between squares, the width of the slice  $g_s$ , and the angle  $\theta_s$  of the slice control the three independent tensor components.

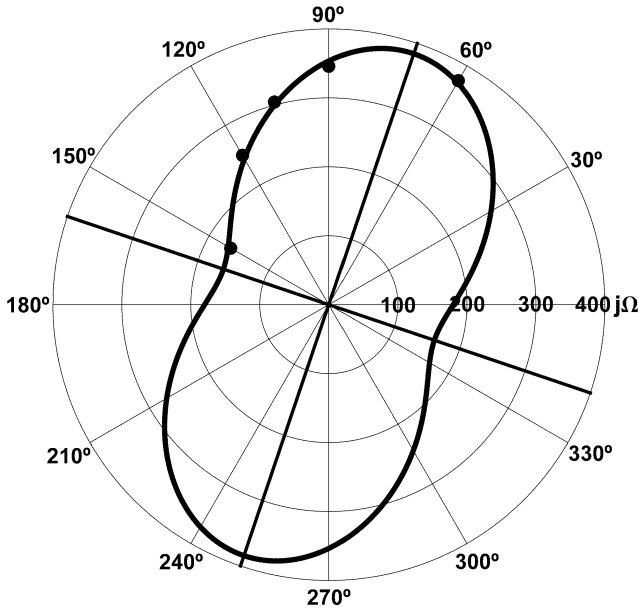


Fig. 8. Plot of effective scalar impedance as a function of surface wave propagation direction  $\theta_k$  for the sliced patch unit cells shown in Fig. 6 ( $g = 0.2$  mm,  $g_s = 0.2$  mm,  $\theta_s = 60^\circ$ ), at a frequency of 10 GHz. Points show results of FastScat computations at propagation angles of  $60^\circ$ ,  $90^\circ$ ,  $105^\circ$ ,  $120^\circ$ , and  $150^\circ$ . Least squares solution of (12) gives the continuous curve, with tensor components  $Z_{xx} = 184.1j \Omega$ ,  $Z_{xy} = 67.6j \Omega$ , and  $Z_{yy} = 361.4j \Omega$ . Principal axes are at  $\theta_k = 71.3^\circ$  and  $\theta_k = -18.7^\circ$ , with principal values of  $384.2j \Omega$  and  $161.2j \Omega$ , respectively.

impedance tensor components  $Z_{xx}$ ,  $Z_{xy}$ , and  $Z_{yy}$  are computed from a least squares solution to (17). With the computed tensor components, (17) can again be used to plot the effective normalized scalar impedance as a function of  $\theta_k$ . Instead of the three components  $Z_{xx}$ ,  $Z_{xy}$ , and  $Z_{yy}$ , the anti-Hermitian impedance tensor may alternatively be described by its principal axes and angle of the principal axes. The principal axes and angles of the impedance tensor are also shown in Fig. 8. (Note that the construction of the tensor hologram requires only the determination

of a given geometry's impedance tensor components; one need never compute the scalar impedance as a function of propagation direction to construct the tensor hologram.)

For a given metal patch geometry, we are able to compute the associated impedance tensor using this characterization method. Implementing a given tensor impedance hologram requires the solution of the inverse problem: for the given tensor impedance determine the corresponding metal patch geometry. We solve the inverse problem by constructing a database of metal patch geometries and associated impedance tensors, and then numerically invert this mapping.

## V. TENSOR SURFACE HOLOGRAPHIC PATTERNING

The tensor impedance hologram generalizes the scalar impedance hologram described above. In the tensor impedance case, the surface electric field and surface current are related through

$$\begin{pmatrix} E_x \\ E_y \end{pmatrix} = \begin{pmatrix} Z_{xx} & Z_{xy} \\ Z_{yx} & Z_{yy} \end{pmatrix} \begin{pmatrix} J_x \\ J_y \end{pmatrix}. \quad (18)$$

The tensor impedance function is constructed from the outer product of the expected vector surface current and the desired outgoing electric field vector. The outer product generalizes the simple multiplicative scalar pattern described in (9). In the scalar case, the desired radiated wave term  $\Psi_{rad}|\Psi_{surf}|^2$  results from the scattering of the surface wave from the modulated impedance pattern. In the tensor case, we desire a radiated vector wave term  $\mathbf{E}_{rad}|\mathbf{J}_{surf}|^2$  resulting from the scattering of a vector surface wave from a modulated tensor impedance pattern. A modulated tensor impedance proportional to  $\mathbf{E}_{rad} \otimes \mathbf{J}_{surf}^\dagger$  creates this radiated vector wave term when illuminated by the reference surface wave  $\mathbf{J}_{surf}$ . (The dagger gives the Hermitian conjugate.) Thus, we have

$$\mathbf{Z} \cdot \mathbf{J}_{surf} \propto \mathbf{E}_{rad} \otimes \mathbf{J}_{surf}^\dagger \cdot \mathbf{J}_{surf} = \mathbf{E}_{rad} \cdot |\mathbf{J}_{surf}|^2. \quad (19)$$

Satisfying energy conservation requires subtracting from  $\mathbf{E}_{rad} \otimes \mathbf{J}_{surf}^\dagger$  its Hermitian conjugate, while satisfying reciprocity requires keeping only the pure imaginary terms. The resulting impedance tensor that satisfies the energy conservation and reciprocity requirements is then

$$\mathbf{Z}(\mathbf{x}) = j \begin{pmatrix} X & 0 \\ 0 & X \end{pmatrix} + j \frac{M}{2} \text{Im} \left( \mathbf{E}_{rad}(\mathbf{x}) \otimes \mathbf{J}_{surf}^\dagger(\mathbf{x}) - \mathbf{J}_{surf}(\mathbf{x}) \otimes \mathbf{E}_{rad}^\dagger(\mathbf{x}) \right). \quad (20)$$

In order to demonstrate an antenna that cannot be implemented with a scalar impedance surface, we designed a tensor impedance surface to scatter currents from a linearly polarized source to produce circularly polarized radiation. For a feed, we used a WR90 (X-band) waveguide, mounted centered along the Y-edge of a 25.4 cm (Y-dimension) by 40.64 cm (X-dimension) surface. We calculated the interference pattern between currents from a point source at the waveguide aperture and a left hand

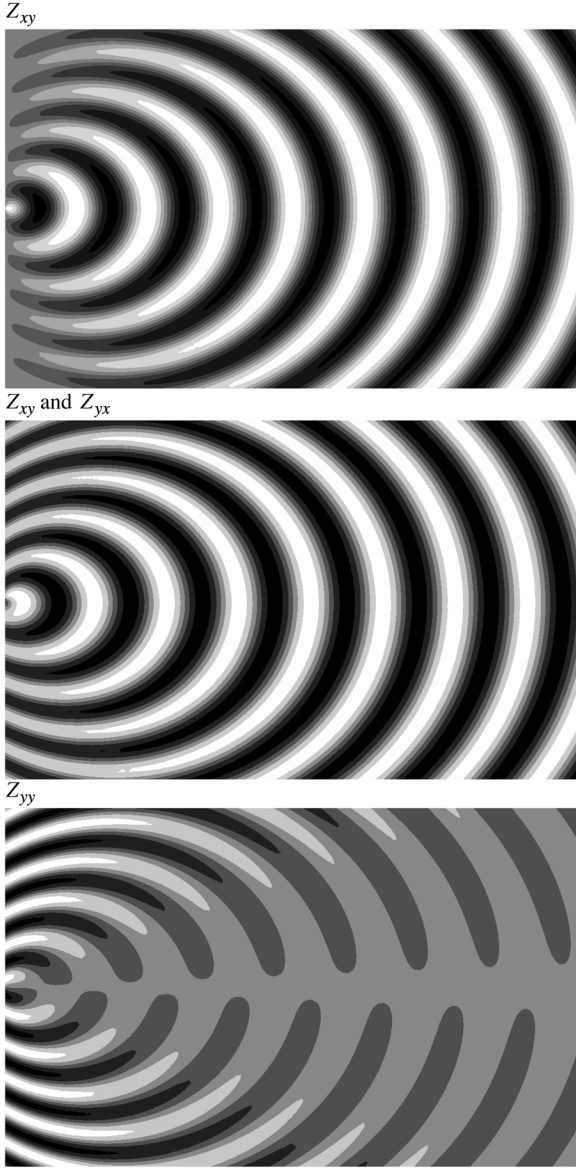


Fig. 9. Tensor impedance components formed from holographic interference. Impedance values are shown on a linear scale, with light areas corresponding to high impedance. The tensor impedance pattern scatters the surface wave from a vertically polarized point source into a circularly polarized plane wave  $45^\circ$  from the normal. The functional dependences are given in (15).

circularly polarized plane wave at  $\theta_L = 45$  degrees. Taking the origin of the coordinate system to be at the point source location and the impedance surface to lie in the X-Y plane, the desired outgoing circularly polarized plane wave has electric field given by

$$\mathbf{E}_{rad}(\mathbf{x}) = \left( \frac{j}{\sqrt{2}}, 1, -\frac{j}{\sqrt{2}} \right) e^{-j\mathbf{k}_L \cdot \mathbf{x}} \quad (21)$$

where  $\mathbf{k}_L = k(\sin \theta_L, 0, \cos \theta_L)$ . The surface current excited by the point source is given by

$$\mathbf{J}_{surf}(\mathbf{x}) = \frac{(x, y, 0)}{r} e^{-jknr} \quad (22)$$

where  $r = (x^2 + y^2)^{1/2}$ . Substituting (21) and (22) into (20), we compute the impedance tensor as a function of position (shown in Fig. 9)

$$\mathbf{Z}(\mathbf{x}) = j \begin{pmatrix} Z_{xx} & Z_{xy} \\ Z_{yx} & Z_{yy} \end{pmatrix}$$

where

$$\begin{aligned} Z_{xx} &= X - M \frac{x}{r} \cos \theta_L \cos \gamma \\ Z_{xy} &= Z_{yx} = \frac{M}{2} \left[ -\frac{y}{r} \cos \theta_L \cos \gamma + \frac{x}{r} \sin \gamma \right] \\ Z_{yy} &= X + M \frac{y}{r} \sin \gamma. \end{aligned} \quad (23)$$

Here  $\gamma \equiv kx \sin \theta_L - knr$ ,  $X$  is the average reactance, and  $M$  is the reactance modulation depth. The impedance tensor given in (23) is the desired functional form for a surface scattering a linearly polarized excitation into a circularly polarized output.

To implement this functional form for the tensor impedance we used the sliced-patch geometry pattern on a 1.27 mm thick Rogers 3010 microwave substrate, with a lattice constant of 3 mm. Using FastScat, we simulated at 10 GHz a range of geometries with  $g$  and  $g_s$  varying from 0.2 mm to 1 mm and 0.2 to 0.5 mm, respectively. The slice angle varied over 360 degrees. With these parameters the FastScat computed major principal axis impedance varied from 116j to 384j Ohms, and the minor principal axis impedance varied from 115j to 161j Ohms. The angle of the principal axes varied over 360 degrees. For the Rogers 3010 substrate, a scaling function was required in order to match the FastScat (or HFSS) computed impedance values to near-field measured impedance values. The reason behind the need for a scaling function to match the measured values to the simulated values, which agree among multiple simulation methods, or to analytical solutions, [18] is still unknown. We constructed a set of uniform scalar impedance surfaces and determined their surface impedances using near-field measurements and FastScat computations. The scaling function is the function mapping FastScat computed impedance values to measured impedance values. The scaling function varied from 1 at low impedance values to 1.37 at high impedance values. The scaled values corresponding to the FastScat computed values given above are 121j to 509j Ohms for the major axis impedance, and 119j to 185j Ohms for the minor axis impedance. Fig. 10 shows the principal axes' scaled impedances for a range of gaps  $g$  and two slice widths  $g_s = 0.2$  mm and  $g_s = 0.5$  mm.

The functional form in (23) requires that the major principal axis impedance vary between  $jX$  and  $j(X + M)$  while the minor principal axis impedance vary between  $j(X - M)$  and  $jX$ . From Fig. 10 we see that it is impossible for the sliced gap structure to satisfy the principal axes' impedance values required by (23). For the sliced gap structure, the principal axes' accessible impedance ranges never overlap. Because we

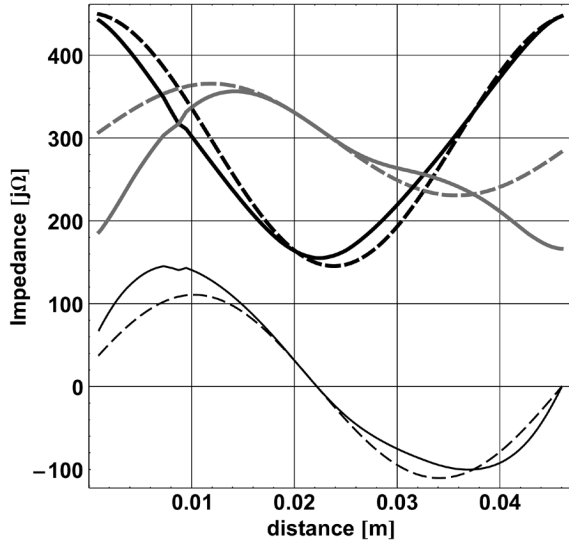


Fig. 10. Tensor impedance components along a one-dimensional slice on the impedance surface. Solid lines are impedance components realized using sliced gap patches; dashed lines are desired impedance components specified by (15). Thick black lines are the  $Z_{xx}$  component, grey lines are  $Z_{yy}$ , and thin black lines are  $Z_{xy}(=Z_{yx})$ .

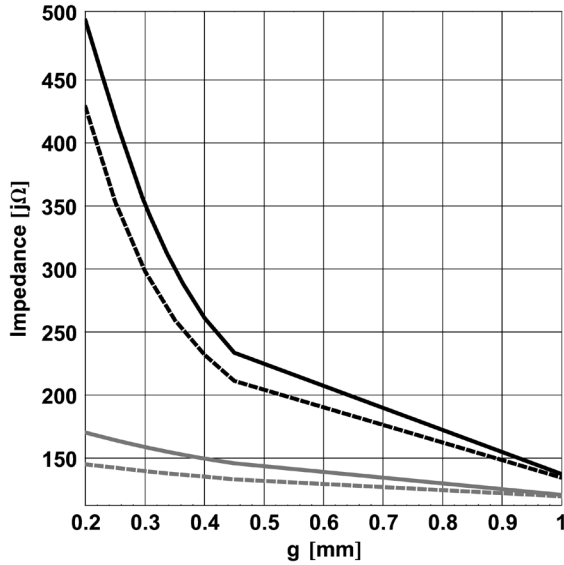


Fig. 11. Major and minor principal axes impedances as a function of gap size for two slice gap widths  $g_s$ , at slice angle  $\theta_s = 90^\circ$ . Black lines are major axis impedances; grey lines are minor axis impedances. Solid lines are for  $g_s = 0.2$  mm; dashed lines are for  $g_s = 0.5$  mm.

are unable to match both principal values of (23) simultaneously, we have chosen to match only the major axis impedance and the angle of the principal axes; the matching can be accomplished by fixing the slice width at 0.2 mm while varying only the gap and the slice angle. Fig. 11 shows the impedance tensor components demanded by (23) and the constructed impedance tensor components matching only the angle and major axis impedance, along a diagonal on the surface. The constructed components match the general trend of the required components. For the structure that we built, the average reactance  $X = 298$  Ohms, and the reactance modulation depth  $M = 226$  Ohms.

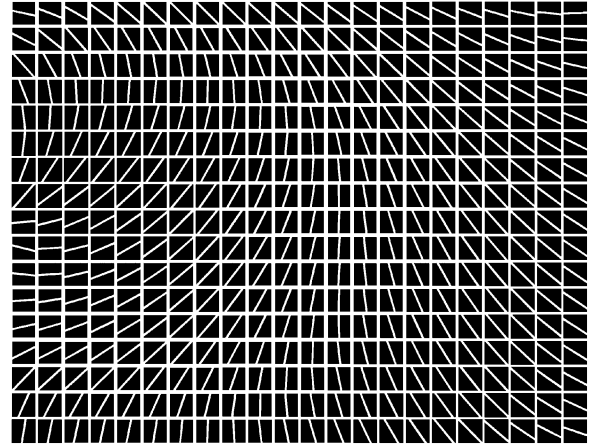


Fig. 12. A portion of the tensor holographic impedance surface of Fig. 8 and (15) implemented using sliced gap unit cells.

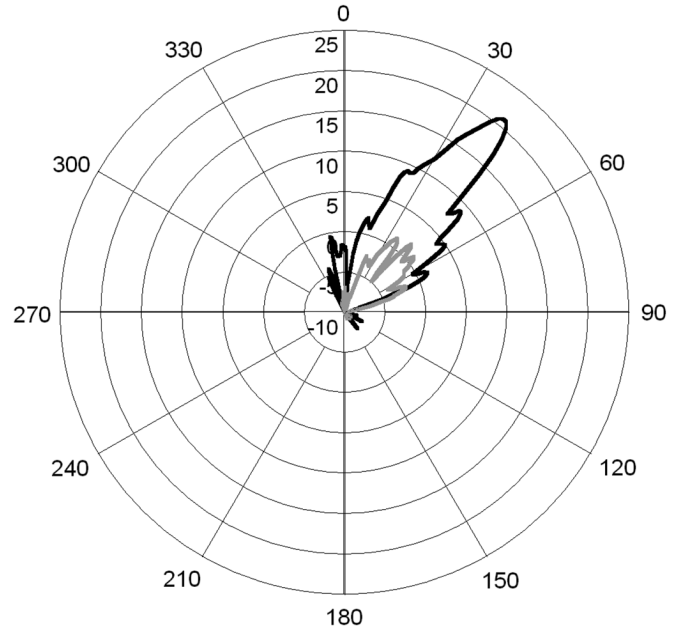


Fig. 13. Measured radiation patterns from monopole antenna placed above the tensor holographic impedance surface. Left-hand circularly polarized radiation is shown in black; right-hand circularly polarized radiation is in grey.

We fabricated and measured the tensor impedance surface pattern shown in Fig. 9, implemented using our sliced patch geometry, for which a small section is shown in Fig. 12. Note that the angle of the slice rotates with each unit cell with increasing distance from the source, which is at the center of the left edge of the figure. Fig. 13 contains plots of the measured far field patterns, in terms of left hand and right hand circular polarization components. The measure left hand circular polarization beam peak gain was 21.8 dB at 38 degrees from the surface normal. At the left hand circular polarization beam peak the right hand circular polarization component was down by 19.6 dB. This measured far field data shows good agreement in terms of polarization purity compared to the computed pattern for the ideal tensor impedance surface, shown in a previous publication [4] but the beam peak is off by 7 degrees. An error in beam angle may be caused by an error in



the calculated phase velocity of the surface wave. This may be due to the fact that the impedance of the tensor surface was not directly measured using the near field technique to determine the scaling function, but instead we applied a scaling function obtained from scalar surfaces.

## VI. CONCLUSION

We have demonstrated that we can build both scalar and tensor artificial impedance surfaces, and that these can be used to design conformal antennas with a range of important properties. Scalar surfaces can be implemented using a simple lattice of square metal patches with variable gap width, while tensor surfaces can be implemented by introducing a slice through the patches having a variable angle. The scalar surface can be designed to scatter a given surface wave into a desired far-field radiation pattern, and the tensor surface extends this concept to provide polarization control. We have used this concept to design and build a surface that can generate a circularly polarized plane wave from a linearly polarized source. It is possible that this work can be extended to include a wide range of alternative geometries that may provide even greater control over the values of the impedance tensor to enable greater accuracy of designs and more control over the radiation pattern.

## REFERENCES

- [1] P. Hariharan, *Optical Holography: Principles, Techniques and Applications*. Cambridge, U.K.: Cambridge Univ. Press, 1996, pp. 11–13.
- [2] D. Sievenpiper, J. Colburn, B. Fong, J. Ottusch, and J. Visher, "Holographic artificial impedance surfaces for conformal antennas," presented at the IEEE Antennas and Propagation Symposium Digest, Washington DC, Jul. 5, 2005.
- [3] J. Colburn, D. Sievenpiper, B. Fong, J. Ottusch, and P. Herz, "Advances in artificial impedance surface conformal antennas," in *IEEE Antennas and Propagation Symposium Digest*, Washington DC, Jun. 9, 2007, pp. 3820–3823.
- [4] B. Fong, J. Colburn, P. Herz, J. Ottusch, D. Sievenpiper, and J. Visher, "Polarization controlling holographic artificial impedance surfaces," in *IEEE Antennas and Propagation Symposium Digest*, Washington DC, Jun. 9, 2007, pp. 3824–3827.
- [5] A. Oliner and A. Hessel, "Guided waves on sinusoidally-modulated reactance surfaces," *IRE Trans. Antennas Propag.*, vol. 7, no. 5, pp. 201–208, Dec. 1959.
- [6] R. King, D. Thiel, and K. Park, "The synthesis of surface reactance using an artificial dielectric," *IEEE Trans. Antennas Propag.*, vol. 31, no. 3, pp. 471–476, May 1983.
- [7] D. Sievenpiper, L. Zhang, R. Broas, N. Alexopolous, and E. Yablonovitch, "High-impedance electromagnetic surfaces with a forbidden frequency band," *IEEE Trans. Microw. Theory Tech.*, vol. 47, pp. 2059–2074, Nov. 1999.
- [8] C. Caloz and T. Itoh, "Transmission line approach of Left-Handed (LH) materials and microstrip implementation of an artificial LH transmission line," *IEEE Trans. Antennas Propag.*, vol. 52, pp. 1159–1166, May 2004.
- [9] C. Caloz, S. Lim, C. A. Allen, and T. Itoh, "Leakage phenomena from negative refractive index structures," in *Proc. URSI Int. Symp. on Electromagnetic Theory*, Pisa, Italy, May 2004, pp. 156–158.
- [10] C. Caloz, T. Itoh, and A. Rennings, "CRLH metamaterial leaky-wave and resonant antennas," *IEEE Antennas Propag. Mag.*, vol. 50, no. 5, pp. 25–39, Oct. 2008.
- [11] L. F. Canino, J. J. Ottusch, M. A. Stalzer, J. L. Visher, and S. M. Wandzura, "Numerical solution of the Helmholtz Equation in 2D and 3D using a high-order Nyström discretization," *J. Comput. Phys.*, vol. 146, pp. 627–663, 1998.
- [12] S. Ramo, J. R. Whinnery, and T. Van Duzer, *Fields and Waves in Communication Electronics*, 2nd ed. New York: Wiley, 1984.
- [13] A. M. Patel and A. Grbic, "A printed leaky wave antenna with a sinusoidally modulated surface reactance," presented at the IEEE Antennas and Propagation Symp., Charleston, SC, Jun. 1–5, 2009.
- [14] R. Dooley, "X-band holography," *Proc. IEEE*, vol. 53, no. 11, pp. 1733–1735, Nov. 1965.
- [15] W. Kock, "Microwave holography," *Microwaves*, vol. 7, no. 11, pp. 46–54, Nov. 1968.
- [16] P. Checcacci, V. Russo, and A. Scheggi, "Holographic antennas," *IEEE Trans. Antennas Propag.*, vol. 18, no. 6, pp. 811–813, Nov. 1970.
- [17] D. J. Hoppe and Y. Rahmat-Samii, *Impedance Boundary Conditions in Electromagnetics*. Washington, DC: Taylor & Francis, 1995, pp. 135–137.
- [18] O. Luukkainen, C. Simovski, G. Granet, G. Goussetis, D. Lioubtchenko, A. Raisanen, and S. Tretyakov, "Simple and accurate analytical model of planar grids and high-impedance surfaces comprising metal strips or patches," *IEEE Trans. Antennas Propag.*, vol. 56, no. 6, pp. 1624–1632, Jun. 2008.



**Bryan H. Fong** received the B.S. degree in physics from Yale University, New Haven, CT, in 1993 and the M.A. and Ph.D. degrees in plasma physics from Princeton University, Princeton, NJ, in 1995 and 1999, respectively.

He is a Senior Research Staff Physicist in the Computational Physics Department, HRL Laboratories, LLC, Malibu, CA. He joined HRL Laboratories in 2001, following postdoctoral research at the National Center for Atmospheric Research. His research has been in nonlinear instabilities in laboratory and astrophysical plasmas, computational electromagnetics, high-order numerical methods, and quantum information.

Dr. Fong is a member of the American Physical Society.



**Joseph S. Colburn** (M'92) received the B.S. degree from the University of Washington, Seattle, in 1992, and the M.S. and Ph.D. degrees from University of California, Los Angeles, in 1994 and 1998 respectively, all in electrical engineering.

Since 1998, he has been with HRL Laboratories, Malibu, CA, where he is currently the Antenna Department Manager in the Applied Electromagnetics Laboratory. At HRL he has worked on millimeter and microwave antennas and circuits for aerospace and automotive applications. From 1995 to 1997, he was with the TRW Space and Electronics Group where he was involved with the design and measurement of satellite antennas. He has over 25 papers published in technical publications and was issued 10 patents.



**John J. Ottusch** was born in Landstuhl, Germany, in 1955. He received the S.B. degree in physics from the Massachusetts Institute of Technology, Cambridge, and the Ph.D. degree in physics from the University of California, Berkeley, in 1977 and 1985, respectively.

In 1985, he joined Hughes Research Laboratories (now HRL Laboratories), Malibu, CA. Until 1994, his research involved experimental investigations of nonlinear optics, including Raman and Brillouin scattering and optical phase conjugation. Since that time he has focused primarily on developing fast, high-order algorithms and software for electromagnetic modeling.



**John L. Visher** received the B.A. degree from the University of California in Santa Cruz, in 1979 and the M.A. degree from Columbia University, New York, in 1981, both in physics.

For over 23 years he has worked in HRL Laboratories, Malibu, CA, and its previous corporate incarnations. He has written more code for more projects than he can or cares to remember. His most recent code models EM in the time domain with novel high order stable and explicit techniques.



**Daniel F. Sievenpiper** (M'94–SM'04–F'09) received the B.S. and Ph.D. degrees in electrical engineering from the University of California, Los Angeles, in 1994 and 1999, respectively.

Since 2010, he has been a Professor at the University of California, San Diego, where his research focuses on antennas and electromagnetic structures. Previously, he was the Director of the Applied Electromagnetics Laboratory at HRL Laboratories in Malibu, CA, where his research included artificial impedance surfaces, conformal antennas, tunable and wearable antennas, and beam steering methods. He has more than 60 issued patents and published more than 50 technical publications.

Dr. Sievenpiper was awarded the URSI Issac Koga Gold Medal in 2008, and in 2009 he was named as a Fellow of the IEEE. In 2010, he was elected to the Antennas and Propagation Society Administrative Committee.